Buddensiek, M.-L., Sheng, J., Crosby, T., Schuster, G. T., Bruhn, R. L., He, R. (2008): Colluvial wedge imaging using traveltime and waveform tomography along the Wasatch Fault near Mapleton, Utah. - Geophysical Journal International, 172, 2, pp. 686—697.

DOI: http://doi.org/10.1111/j.1365-246X.2007.03667.x

Geophys. J. Int. (2008) **172,** 686–697 doi: 10.1111/j.1365-246X.2007.03667.x

Colluvial wedge imaging using traveltime and waveform tomography along the Wasatch Fault near Mapleton, Utah

M.-L. Buddensiek,* J. Sheng,† T. Crosby,‡ G. T. Schuster, R. L. Bruhn and R. He§

Department of Geology and Geophysics, University of Utah, Salt Lake City, Utah, USA

Accepted 2007 October 24. Received 2007 October 24; in original form 2006 December 21

SUMMARY

Four high-resolution seismic surveys were conducted across the Wasatch Fault Zone near Mapleton, Utah. The objective was twofold: (1) To use velocity tomograms and reflection images to delineate fault structures and colluvial wedges to more than twice the depth of the Mapleton Megatrench excavated by URS personnel, (2) to assess the strengths and limitations of traveltime and waveform tomography by synthetic studies and comparison of the tomogram to the ground truth seen in the Megatrench log. Four out of the five faults within the trench area are accurately identified in the migrated image and in the tomograms, and the main fault's dip angle is estimated to be between 71 and 80°. Two additional faults are interpreted outside the trench. The faults can be delineated down to 30 m below the surface, which is 20 m deeper than the excavated trench. Five out of six colluvial wedges found in the trench log were seen as low-velocity zones (LVZs) in the tomogram, however the biggest colluvial wedge could not be identified by either tomography method. Waveform tomography prevailed over ray-based traveltime tomography by more clearly recovering the faults and LVZs. A newly discovered LVZ at a depth of 18–21 m below the surface possibly represents a colluvial wedge and is estimated to be less than 21 000 years old. If this LVZ is a colluvial wedge, the earthquake history obtained by trenching can be extended from 13 500 to 21 000 yr with seismic tomography. Our results further demonstrate the capability of tomography in identifying faults, and show that waveform tomography more accurately resolves colluvial wedges compared to traveltime tomography. However, despite the successful recovery of most faults and some, but not all, colluvial wedges, both tomography methods show many more LVZs besides the wedges, so that an unambiguous interpretation cannot be made. A major part of the ambiguity in the tomograms is due to the many major faults, which result in an uneven raypath coverage as our synthetic studies show. Hence, seismic trenching will be more successful at simple fault geometries. However, even under optimal conditions there will be some ambiguity in the interpretation, so that detected LVZs should be drilled, cored, and dated to determine the history of the ancient earthquakes.

Key words: Paleoseismology; Seismic tomography.

1 INTRODUCTION

The Wasatch fault is a 343-km long active normal fault that has not experienced a surface-faulting earthquake in the past 400 yr (Machette *et al.* 1991). It is divided into at least 10 segments, ranging in length from 11 to 70 km. Being the most active faults in Utah, the central segments (Fig. 1) of the Wasatch fault (Brigham City, Weber, Salt Lake City, Provo, and Nephi segments) are the most likely sources for the next large earthquake (Christenson 2004). The combined average recurrence time for large earthquakes ($M > 7$) on any of the five central segments of the Wasatch Fault Zone (WFZ) is 350 yr (McCalpin & Nishenko 1996). At Mapleton, Utah on the Provo Segment the average recurrence interval is estimated to be 1100 to 1600 yr (Olig *et al.* 2005). Trench results constrain the timing of the three most recent surface-faulting events at 618 (±30) yr B.P., 2841 (±72) yr B.P. and 5481 (±152) yr B.P. (McCalpin & Nishenko 1996).

Studies investigating the paleoseismicity of normal fault zones (like the WFZ) traditionally involve geological mapping of Quaternary deposits, analysis of fault scarp morphology, trenching and coring (McCalpin 1996). Geophysical methods, such as seismic reflection and refraction, GPR and resistivity surveys have been widely used to map subsurface geology such as fault locations, geometries

*Now at: Geoforschungszentrum Potsdam, Potsdam, Germany.
†Now at: Nexus Geoscience Inc., Houston, Texas, USA.
‡Now at: Subsurface Surveys, California, USA.
§Now at: Paulsson Geophysical Services Inc. (P/GSI), Brea, California, USA.

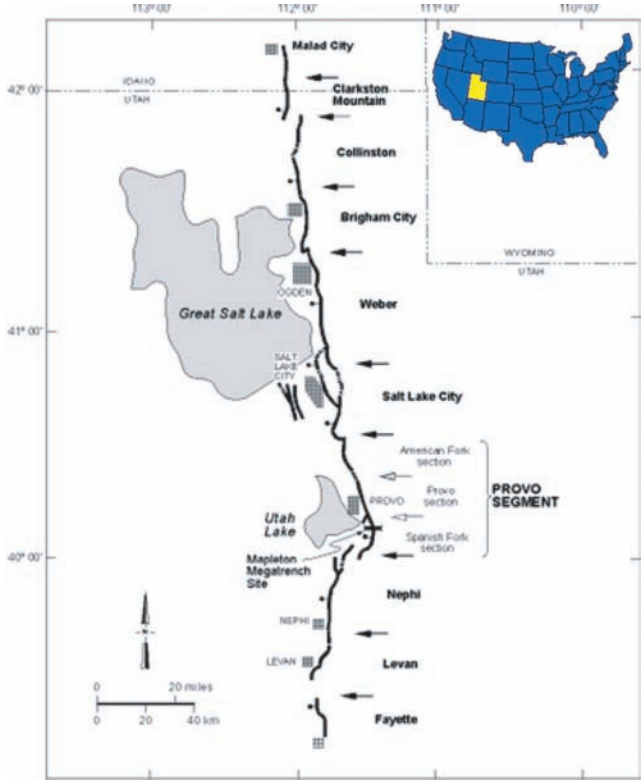

Figure 1. Map of Northern Utah with the outline of segments of the Wasatch Fault Zone (WFZ). The survey site is near Mapleton, Utah.

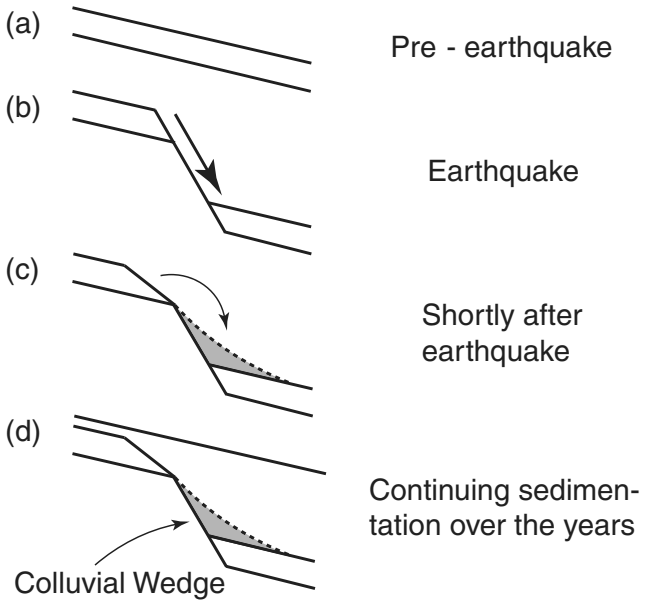

Figure 2. Depiction of the creation of a colluvial wedge. (a) Cross-section of layered earth. (b) Rupture of normal fault earthquake, with scarp rubble filling up on the footwall of the fault. (c) A new layer forms on top of the rubble, preserving the shape of the colluvial wedge (Morey & Schuster 1999).

and displacements (McCalpin 1996; Meghraoui *et al.* 2000; Chow *et al.* 2001, and many others). To facilitate paleoseismic studies, trenches are excavated across normal faults to precisely determine the location and shape of colluvial wedges, which are wedge-shaped deposits that accumulate at the base of a fault scarp following a surface rupturing event (Fig. 2). They are a characteristic geological signature of an ancient dip-slip earthquake (McCalpin 1996), and can be used to determine the recurrence interval by carbon dating colluvium samples. Fig. 3 shows a photograph of a colluvial wedge in the Mapleton Megatrench. If trenching is not applicable (too costly, too remote area) or as an advance surveying tool, GPR surveys can be used to determine the location and geometry of normal, oblique and strike-slip faults (Chow *et al.* 2001; Bilham 1985; Bilham & Seeber 1985; Smith & Jol 1995; McCalpin 1996). Bilham (1985) and Bilham & Seeber (1985) found that coarse colluvium and fan alluvium did not possess dielectric layering, and so returned few reflections. However, they did detect pre-historic colluvial wedges at the Borah Peak, Idaho fault scarp, because of their underlying clay-bearing buried soils that formed during interseismic periods caused reflections. Also, Chow *et al.* (2001) detected a colluvial wedge in eastern Taiwan using a 200 MHz antenna at 5-m depth. Unfortunately, the trenching depth and GPR penetration with reasonable resolution is limited to depths of no more than 10 m and so provides earthquake recurrence information no later than 10^3 to 10^4 yr along the WFZ. For example, the Mapleton Megatrench, excavated in 2003, uncovered 13 500 yr of sedimentation in just over 9 m trench depth (Olig *et al.* 2005). But there is mounting evidence that earthquake recurrence intervals must be sampled over time scales on the order of 10^5 yr to fully reveal their spectral characteristics (Kanamori & Brodsky 2001).

Figure 3. Photograph of a colluvial wedge at the Mapleton Megatrench. The solid and the dashed lines delineate the fault plane and the colluvial wedge, respectively.

To extend the depth of paleoseismic investigation, high-resolution seismic tomography was proposed as a new tool for imaging colluvial wedges (Morey & Schuster 1999). The principle conjecture of this procedure is that colluvial wedges are characterized by detectably lower *P*-wave velocity than the surrounding alluvium. Hence, colluvial wedges that have encountered soil development or other compaction, which increases its *P*-wave velocity to that of the surrounding sediment, will not be easily detected by seismic tomography. Also, singular colluvial wedges within packages that are not separated by alluvium cannot be distinguished from each other; they are resolved as packages of colluvial wedges.

The resolution of seismic tomography using a sledge hammer source can sometimes be used to unambiguously identify colluvial

wedges of 3-m height and 6-m width (Mattson *et al.* 2003; Sheley *et al.* 2003) down to a depth of 10 m. Hereby, the thickness of the colluvial wedge is proportional to the fault displacement, and the depth interval between neighboring wedges determines the recurrence interval of earthquakes depending on the sedimentation rate through time. However, smaller or deeper colluvial wedges or packages of colluvial wedges may not be resolved unambiguously in size and shape. Nevertheless, low-velocity zones (LVZs) can be an indication of colluvial wedges, and so guide the decision for the location of drill sites. Several seismic surveys over the Wasatch and the Oquirrh Fault Zones showed that seismic trenching, that is refraction tomography, can provide deeper (20 m) albeit less resolved images of fault systems and their colluvial wedges than the standard excavation and logging of trenches across faults (Morey & Schuster 1999; Sheley *et al.* 2003; Mattson 2004). The repeated success of this tomographic method along the Wasatch and Oquirrh faults suggested that it can be used as a complimentary method to any trench study as it has a lower resolution than trenching but allows to identify deeper structures than the trench itself. Seismic trenching is also much cheaper than trenching is, for example our 84-m 2-D survey took three persons 1 day in the field, and one person 10 days of processing.

The objective of this research is to use seismic imaging methods to identify faults and delineate the location and shape of buried colluvial wedges or packages over the Wasatch Fault near Mapleton, Utah. It is expected that the image depth obtained by traveltime and waveform inversion, and by reflection migration should be at least twice as deep as the nearby trench (<10 m), so that the information about the earthquake history obtained by trenching can be extended to earlier times.

In the summer of 2002, University of Utah students performed a 2-D high-resolution refraction experiment at the proposed megatrench site near Mapleton, Utah (Figs 1 and 4). The depth of the imaged section was more than 25 m with a horizontal extension of 83.5 m. Following these experiments, the URS Corporation excavated in the summer of 2003 the Mapleton Megatrench, 'with the purpose of exposing evidence for prehistoric earthquakes (paleoseismicity) back in time to more than 11 000 yr ago, doubling the length of the paleoseismic record for the Provo segment' (Olig *et al.* 2004). The fault locations of the 2003 trench log coincide with those of the hypothetical fault model based on the migrated image of the Pre-Trench data to ± 1 m. Moreover, the faults are extended from 10 to 30 m depth and a possible colluvial wedge is seen at a depth of 18–21 m below the surface. Three additional seismic experiments were conducted in the open trench, revealing a 15 per cent velocity reduction in the shallow subsurface due to the excavation. One of these 'Post-Trench' tomograms resolves a 70–80° fault dip of the main synthetic fault.

Figure 4. Aerial view of the survey site. Delineated are the survey site (yellow) of both seismic experiment and the trench, the WFZ (red) and the Lake Bonneville shoreline (blue).

This paper is presented in four sections: First, the seismic experiments and the inversion methods are described. In the second part, synthetic tests demonstrate the capability of resolving faults and colluvial wedges in tomograms. The third section presents the results of migration and tomographic imaging for the Pre-Trench and Post-Trench data sets; and the fourth section presents the conclusions.

2 SEISMIC SURVEYS AND DATA PROCESSING

A series of 2-D high-resolution seismic surveys were carried out near Mapleton, Utah perpendicular to the Provo Segment of the Wasatch Fault (Fig. 1). The aerial view in Fig. 4 shows the WFZ, the Lake Bonneville shoreline and the survey site. The data are classified as Pre-Trench and Post-Trench depending on whether they were collected prior to or after the excavation of the trench in July 2003, respectively. Tables 1 and 2 summarize the acquisition and source-receiver parameters, respectively. In all standard surface refraction surveys, the shot locations coincided with the geophone locations in order to apply a reciprocity quality control method to the traveltime picks (Morey & Schuster 1999).

In September 2002, an 83.5-m long seismic survey (Pre-Trench) was conducted using 168 geophones and 168 shots. The objective was to use phase-shift migration, traveltime tomoraphy and early arrival waveform (EAW) tomography (Sheng *et al.* 2006) to delineate the shape and location of colluvial wedges and the fault geometry to a depth of more than 30 m, that is more than 15 000–20 000 yr B.P.. In addition, the strengths and limitations of both tomography methods were assessed by comparing the tomograms to the position of faults identified in the migrated image and wedges extracted from

Table 1. Acquisition parameters for all surveys.

Shot-receiver spacing:	0.5 m
Recording Instruments:	40-Hz vertical-component geophones 48-channel BISON 120-channel BISON
Source:	16-pound sledgehammer, 5 shots stacked at each shot point in order to improve the S/N ratio

Table 2. Parameters for seismic surveys. The 'no. of traveltimes' column displays the number of traveltimes that passes the quality check versus the total number of traveltimes. Picking errors were estimated to be about 3 ms for all data sets (Pre- and Post-Trench incl. Top-, Middle- and Crossbench (TB, MB and CB, resp.).

Survey	No. of shots	No. of receivers	Shot/receiver spacing	No. of traveltimes
Pre-Tr.	168	168	0.5 m	27 662 / 28 224
Post-Tr.: TB	120	48	0.5 m	4644 / 5040
Post-Tr.: MB	120	120	0.5 m	13 638 / 14 400
Post-Tr.: CB	240	168	0.5 m	17 081 / 20 160

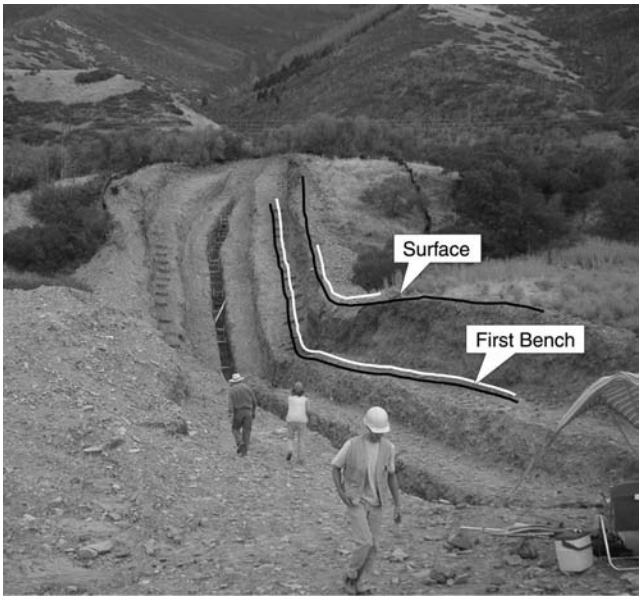

Figure 5. Photograph of the Mapleton Megatrench. The receiver lines of the seismic survey in the trench are delineated in white and the shot lines in black. The Pre-Trench seismic survey was nearly coincident with the black line along the top bench.

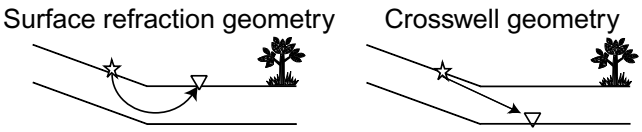

Figure 6. Sketch of standard surface refraction raypaths versus crossbench raypaths.

the trench log of Olig *et al.* (2004) of the Mapleton Megatrench (excavated by URS Corporation in August 2003).

The trench was approximately 84 m long and 10 m deep perpendicular to the fault (Olig *et al.* 2005) and nearly coincident with the Pre-Trench experiment. Three additional seismic surveys were performed in the open trench. The photograph in Fig. 5 illustrates the geometry of the trench with the geophone and shot lines indicated by solid white and black lines, respectively, along the 'top' and the 'middle' benches. Forty-eight geophones were deployed on the ground surface next to the trench (denoted as 'top bench') centred over the base of the fault scarp, and 120 geophones were deployed on the middle bench of the trench. The first source line was located on the top bench, parallel to the 48-geophone-line, but extending to both sides for a total of 120 shot locations. The vibrations from each shot were simultaneously recorded by all 168 geophones.

The data recorded by the 48 geophones on the top bench form a standard surface refraction profile with a total of 5040 recorded traces. The objective was to determine the modification of the subsurface velocities caused by the excavation of the trench.

The top and the middle benches are roughly parallel and have an approximate vertical separation of 4 m, so that the data recorded by the 120 geophones on the middle bench with the sources at the top bench form a cross-well experiment with the wells rotated by 90° (Fig. 6). Hence, this survey is denoted as the Crossbench survey. The reverse-shooting geometry was recorded with the second shot line of 120 source locations at the middle bench and 48 geophones recording at the top bench, so that 14 440 traces were collected. The objective was to achieve a better horizontal resolution of the near surface in order to determine the horizontal extension and the velocity of the colluvial wedge found by trenching between the top and the middle bench.

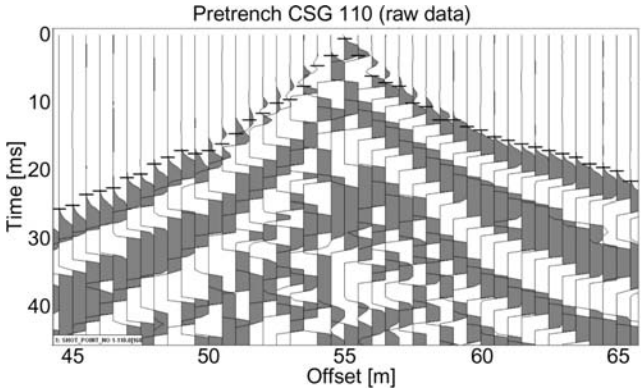

Figure 7. Zoom view of the near offset traces of the common shot gather 110. The traveltime picks (horizontal bars) are below the airwave (high-frequency wavelet).

The source locations of the second shot line coincide with the geophone positions on the middle bench, so that another standard surface refraction experiment was acquired on the middle bench (i.e. 'Middle-Bench' data). The objective here was to achieve a better resolution of the fault complex underneath the middle bench than provided by the Pre-Trench tomogram.

The first step in tomography processing is to pick first-arrival traveltimes, where special attention is paid to the airwave arriving earlier than the *P*-wave as seen in the common shot gather in Fig. 7. The airwave is easily recognized by its 333 m s^{-1} velocity and its high frequency relative to the refraction arrival, so that the *P*-wave can be picked as the wave arriving later in time at the near offset geophones. For quality control, a reciprocity test was performed: Traveltime pairs t_{ij} and t_{ji} were rejected, if they did not satisfy the reciprocity condition $t_{ij} = t_{ji}$ to within a tolerance of 3 milliseconds. Here, t_{ij} represents the first-arrival traveltime pick for a source at the *i*th position and a receiver at the *j*th position, where the shot point locations are coincident with the receiver locations (Morey & Schuster 1999).

The remaining traveltimes that passed the reciprocity test (Table 2) were inverted using the multiscale SIRT algorithm described in Morey & Schuster (1999) and Nemeth *et al.* (1997), which incorporates multiscale smoothing filters (see Table 3 for inversion parameters). Briefly, the first-break arrival times are computed for an initial slowness model using a finite-difference solution to the eikonal equation (Qin *et al.* 1992). The misfit function, which is defined as the sum of the squared traveltime differences between the observed and the computed traveltimes, is calculated and the

Table 3. Smoothing schedule for Pre-Trench, Top-Bench, Middle-Bench, and Crossbench data. The smoothing filter sizes (Sm) are given in number of cells.

Experiment	Pre-Trench	Post-Trench: Top-Bench	Post-Trench: Middle-Bench	Post-Trench: Crossbench
Grid size	0.25 m	0.25 m	0.25 m	0.25 m
Sm 1 (it. no.)	40 × 25 (1)	40 × 25 (3)	40 × 25 (2)	40 × 40 (1)
Sm 2 (it. no.)	25 × 15 (2)	25 × 15 (3)	25 × 15 (1)	25 × 25 (1)
Sm 3 (it. no.)	15 × 10 (2)	15 × 10 (3)	15 × 10 (2)	15 × 15 (2)
Sm 3 (it. no.)	10 × 6 (5)	10 × 6 (6)	10 × 6 (2)	10 × 10 (2)
Sm 4 (it. no.)	N/A	N/A	N/A	6 × 6 (2)
RMS resid/tr	1.7	1.0	2.5	1.6

slowness model is iteratively updated by a gradient optimization method. The spatial smoothing filters allow the algorithm to converge with a smaller number of iterations by starting the iteration with a coarse-grid model. After about 5 iterations the smoothing filter size is halved, which results in a better spatial resolution. However, the size of the filter was never allowed to be smaller than half the dominant wavelength (3 m) of the source wavelet. Also, the ratio of the number of traveltimes to the number of effective unknowns was never below 3:1.

For comparison, we also present tomograms that were computed by using an early arrival waveform inversion algorithm (EAW). Waveform inversion not only uses the traveltimes but also the waveforms of the early arrivals to compute a velocity distribution, which inherently results in a better resolution of the velocity model (Sheng 2004; Sheng *et al.* 2006). The waveform inversion generates a synthetic waveform, which simulates typical waveforms for the early arrivals. As in traveltime tomography, the traveltimes and the waveforms of an initial velocity model are computed using the acoustic wave equation rather than a ray tracing method. A misfit function is computed and the velocity model is updated by backprojecting the waveform residual along the wavepaths.

To facilitate the interpretation, a moving average filter is applied to some of the tomograms as indicated. In order to account for topography, the moving average filter is modified, such that

$$avg(x, z') = \sum_{i=-25}^{25} d(x + i, z')/51, \tag{1}$$

where $d(x, z)$ is the velocity at the grid positions (x, z) of the tomogram, and $z' = z + elevation(x)$. For highboost filtering the difference between the velocity of the tomogram and the average value is divided by the average value:

$$d_{\text{filter}}(x, z) = (d(x, z) - avg(x, z))/avg(x, z). \tag{2}$$

Additionally, a phase-shift migration algorithm was applied to the Pre-Trench reflection data: First, the seismic data recorded on the topographic surface were redatumed to a flat surface using the technique outlined by Hill & Wuenschel (1985). Then, several traces around the zero-offset position were stacked for each common midpoint gather, and finally this section was inserted into a conventional split-step Fourier migration algorithm (Stoffa *et al.* 1990) with velocities taken from the traveltime tomogram.

3 TOMOGRAPHY RESULTS FOR SYNTHETIC DATA

Synthetic tests will now be presented that suggest that the steep topography of the Mapleton site is unlikely to have affected the inversion result in the interpretable area, whereas the number of faults encountered at the site decreased the resolution capabilities of seismic tomography considerably. These results provide a sensitivity test of the computed tomogram as a function of dipping refractors (fault planes), and LVZ (colluvial wedges). The synthetic tests consist of three experiments, all of which have a source/receiver geometry identical to that of the Pre-Trench experiment. The input data consist of first-arrival traveltimes generated by ray tracing the synthetic model.

In order to show the ability of the inversion to resolve simple structures, the first model (Fig. 8) is a vertical gradient model with only one normal fault, simulated by a laterally discontinuous velocity change, and one LVZ that resembles a colluvial wedge at the near surface. The tomogram recovers the model velocities very well

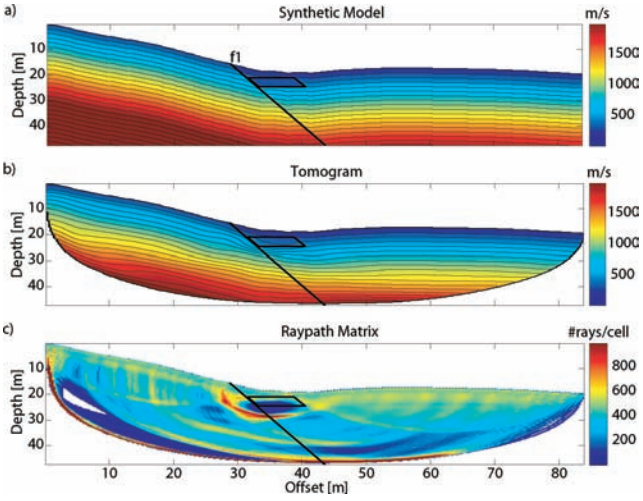

Figure 8. Model 1: (a) Linear gradient velocity model with one fault and one LVZ. (b) In the tomogram, the LVZ is resolved as a zone of a lower vertical velocity gradient. (c) In the raypath matrix, the rays avoid the LVZ to cast a ray shadow.

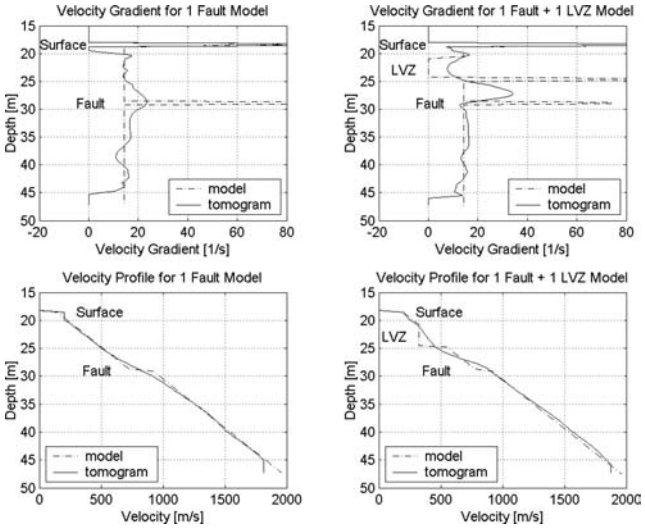

Figure 9. Velocity and gradient profiles of a model containing one fault (left panels) and the model 1 containing one fault and one LVZ (right panels) at the 35-m offset. Velocity discontinuities are identified by high gradients for both models. For model 1, the velocity gradient at the depth of the LVZ is significantly lower than above or below.

down to a depth of 30 m below the surface. The fault is imaged as a gradual velocity variation, while the raypath matrix is characterized by a nearly uniform distribution of rays. However, the rays focus on the footwall side of the fault plane which results in fewer raypaths visiting the hanging wall side. At the location of the fault, this figure also clearly illustrates decreasing resolution with depth. The fault at depth is imaged as a very small velocity drop, since almost no rays pass vertically through the cells at great depths. The velocity of the wedge is on average 15 per cent lower than the background velocity. Obviously, the rays avoid the LVZ, resulting in a smaller vertical velocity gradient in the tomogram.

In Fig. 9, the velocity and gradient profiles of this model at 35-m offset are compared to profiles of a model without the LVZ at the 35-m offset. The graphs for the same model without a LVZ show that the strong gradient at the fault results in a broader and

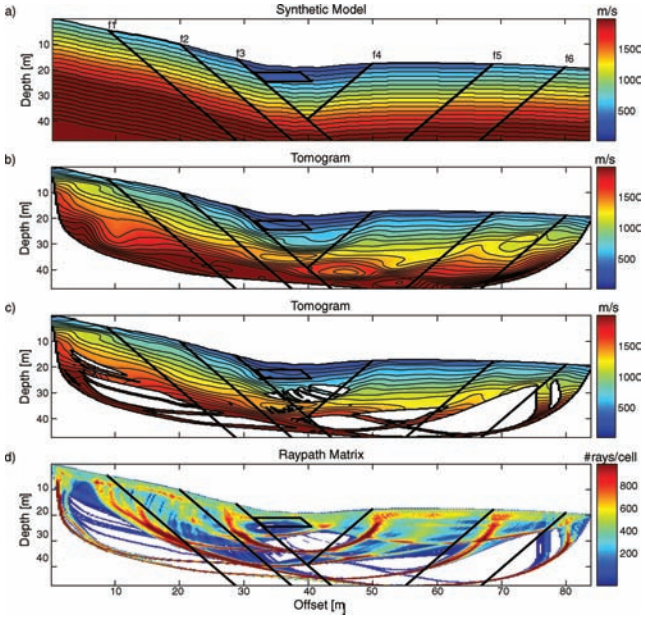

Figure 10. Model 2: (a) Linear gradient velocity model with six faults and one LVZ. (b) In the tomogram, the area between the faults f3 and f4 indicates two LVZs: The minor one is at the actual location of the LVZ and a bigger one, albeit false, is next to it at the 41-m offset and 28-m depth. (c) Ignoring cells with no raypath coverage reduces the distorted areas, including the bigger, false LVZ. (d) Raypath matrix. The areas of ray focusing correspond to actual fault locations.

less pronounced peak in the tomogram, that is the velocity increases gradually rather than instantaneously. Here, the profiles on the right panels intersect the LVZ. The gradient of the model shows the sharp boundaries of the wedge, whereas the inversion smoothed those gradients, so that the sharp contrast in velocity is not recovered. However, the gradient is significantly smaller inside the LVZ than above or below. The velocity discontinuities at the bottom of the colluvial wedge and at the fault, which is 4 m below, are not resolved as single events, but are smeared over these 4 meters.

The second synthetic model mostly imitates the subsurface complexity found at the survey site. It incorporates six faults (f1–f6) and one LVZ as seen in Fig. 10. The identification of faults in a tomogram can be strongly supported by the areas of enhanced focusing in the raypath matrix. The disadvantage of this enhanced ray focusing is that other areas are not penetrated at all. Fig. 10(b) shows the distortion of the velocity distribution in areas of no coverage, which therefore have to be ignored in the interpretation. In order to simplify the comparison between the model and the reliable areas in the tomogram, the cells with fewer than eight ray visits are concealed in Fig. 10(c). Theoretically two visits are sufficient to reliably determine the velocity of a cell, as long as the rays come in from different directions, but in our case the rays visiting a cell often have the same orientation. Thus, we assume that of a certain number of rays visiting a cell, at least two of them have a sufficiently different orientation. This limiting number is picked by eyeball. When cells with more frequently visits are blocked, reliable information is lost, and with fewer visits unreliable information is left for interpretation. Synthetic studies allow a good judgement since we know the real structures and a limit of eight visits appears to be a good threshold. Hence, the remaining areas are left for interpretation:

The area between the faults f3 and f4 in Fig. 10(b) indicates two LVZs: The minor one at the actual location of the LVZ and a bigger one, albeit false, next to it at the 41-m offset and 28-m depth. Again, the distorted areas, including the bigger, false LVZ, have been visited fewer than eight times, whereas the velocities of the more frequently visited cells satisfactorily recovered the faults and the LVZ of the synthetic model. This image demonstrates that the inversion recovered the model down to a depth of 20–25 m below the surface.

The third synthetic model has an additional LVZ at 38 m depth (Fig. 11). The objective was to see whether the six faults defocusing the rays inhibit the resolution of a LVZ at this depth. Of course the LVZ is not meant to simulate a colluvial wedge at this very unlikely position in the footwall of the first antithetic fault f4. After concealing the unvisited cells, the lower velocity gradient of the second LVZ still remains, whereas the misleading distorted areas disappear. Additionally, this third model was inverted using EAW tomography. The resulting tomogram and three selected resolution diamonds (Sheng & Schuster 2003) are shown in Figs 11(e) and (f). Faults and LVZs are resolved more clearly than in traveltime tomography, although the lower LVZ is shifted to the right. According to their colour, the resolution diamonds show the lateral and horizontal resolution limits (i.e. no velocity anomaly smaller than the cell can be resolved) at selected points at the centre of the stars. These limits (Sheng & Schuster 2003) account for the bandlimited nature of the source wavelet and the source-receiver aperture. The red diamond therefore shows that the vertical resolution is too poor to have precisely imaged the LVZ shown in the tomogram, whereas the blue diamond is just small enough to have resolved its LVZ.

This synthetic study shows that faults and LVZs can be imaged by seismic tomography and that the raypath matrix can be essential for interpreting faults in a traveltime tomogram. In order to interpret faults and LVZs in a tomogram and a raypath matrix, we follow eight rules:

(i) A sharp lateral gradient along a steeply dipping line in the tomogram indicates the possible presence of a fault.

(ii) A focusing of raypaths on the footwall side of the fault strongly supports the interpretation of a fault. The exact location of the fault interpretation is determined by its expression in the tomogram.

(iii) If only the raypath matrix indicates a fault by a focusing of raypaths, the exact location cannot be determined and the fault plane is interpreted at the focused raypath.

(iv) Basic knowledge of geology should guide the interpreter (e.g. it is unlikely to find a synthetic fault in the flat portion of the section).

(v) The borders of a tomogram are mostly disturbed by edge effects, therefore structures seen in the border area can mislead the interpretation.

(vi) Faults, LVZs and other velocity variations lead to an uneven raypath coverage, that is to focusing of raypaths and to areas of no or little raypath coverage.

(vii) Cells that are not visited by any or only few rays (in this case, fewer than eight rays) contain no reliable velocity information. They are not necessarily LVZs.

(viii) LVZs are resolved as zones with a lower vertical velocity gradient and less raypath coverage.

4 TOMOGRAPHY RESULTS FOR FIELD DATA

Tomographic results for inverting data from the four experiments described above are presented and compared to a trench log

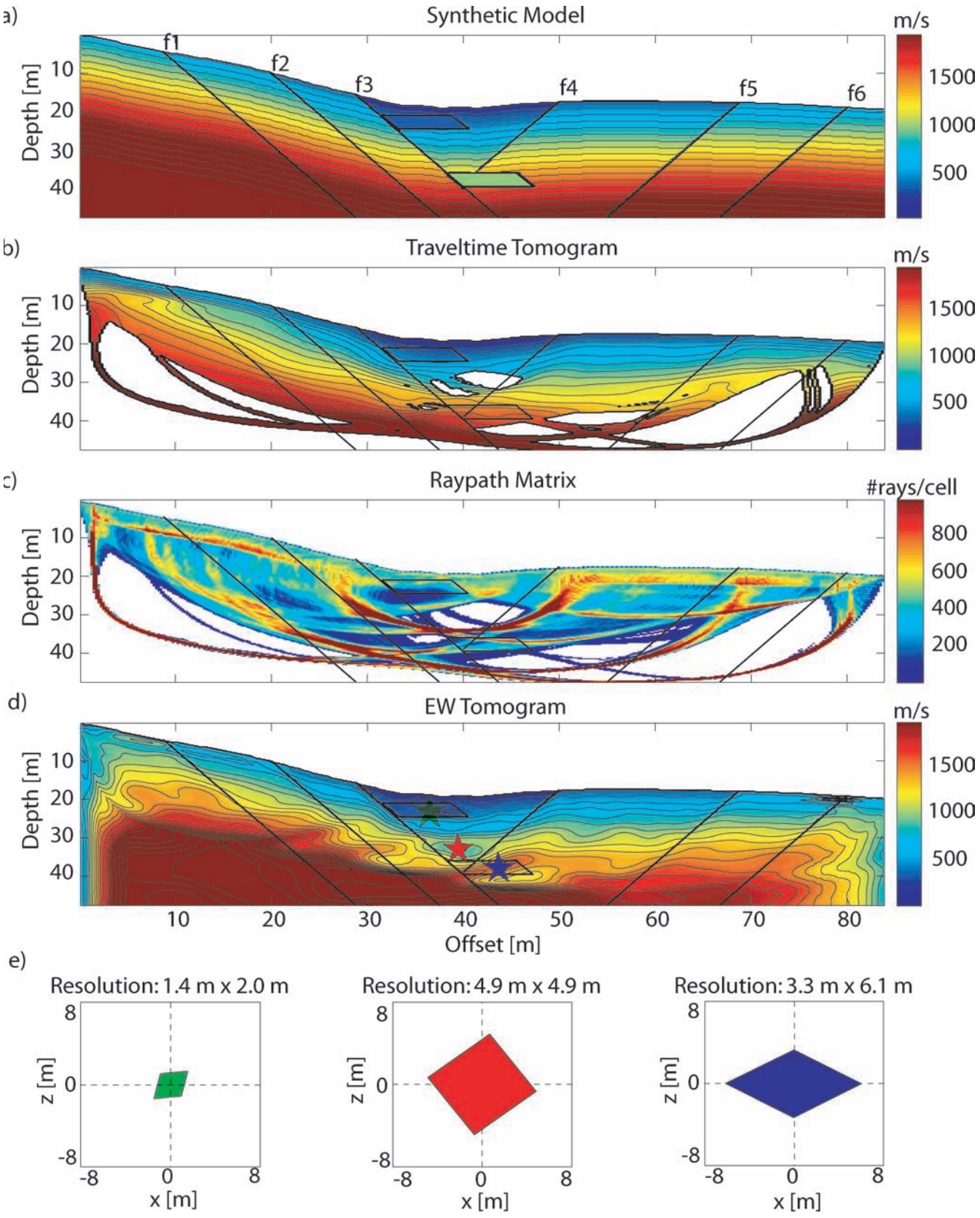

Figure 11. Model 3: (a) Linear gradient velocity model with six faults and two LVZs. (b) The imprint of the deeper LVZ is comparable in magnitude and size to the distortion. (c) Ignoring cells with no raypath coverage reduces the distorted areas, including those around the deep LVZ, but the LVZ remains resolved. (d) Raypath matrix. (e) The EAW Tomogram shows a lot more detail and shows more pronounced faults and low velocity zones. (f) The resolution diamonds show the orientation and size of the resolution limits at the locations of the equally colored stars in (e). The red resolution diamond shows that the resolution is about 10 m, so that the closure of contour lines cannot be interpreted since it is much smaller.

extract (Fig. 12a). The spatial coordinates for the geophone and shot positions of the trench surveys, which outline the top and middle benches, and several coordinates for two colluvial wedges and three faults in the trench were recorded by a tachymeter (solid lines). Additionally, two faults and four LVZs were approximately located (dashed lines). Unfortunately, the trench log extract has not yet been rectified onto an absolute coordinate system, so that this rough outline of the grey colour faults and colluvial wedges may have an offset uncertainty of ± 2 m in each direction. The complete record of the trench log has not been published yet and is owned by URS Corp and the Utah Geological Survey.

4.1 Pre-trench tomographic results

The trench log extract, the results of the phase-shift migration, the traveltime and the early-arrival waveform inversion of the Pre-Trench data are shown in Fig. 12 on the left panels, and their interpretation images on the respective right panels. The asterisks (*) denote close proximity to faults and colluvial wedges (and bioturbation) known from the trench log extract (a).

From the synthetic studies we learned that faults impede an even raypath coverage and complicate the interpretation of tomographic images. To unambiguously identify those faults before interpreting the tomogram, we phase-shift migrated the Pre-Trech data (Fig. 12b) using Stoffa *et al.*'s (1990) split-step Fourier migration algorithm. We identified six faults, four of which (f3*–f6*) coincide very well with faults mapped in the trench log extract (a). The two others (f1 and f7) are located outside the trench area. Fault f2 known from the trench log has not been resolved by the migration, nor by either inversion method, which indicates a very small offset and narrow fault zone.

On the traveltime tomogram (c-h), faults can be interpreted following the criteria from the previous section, although their location remains somewhat imprecise compared to the migrated image (b). The six fault locations taken from the migrated section, however, agree very well with likely locations indicated by the tomogram. Both inversion methods mapped f3*–f6* correctly. Faults f1 and f7 detected by migration are also resolved by traveltime (f1, f7) and waveform tomography (f1). In the EAW image (j), a low-velocity area obscures the location of f7 and shifts it towards the 80-m offset. These inconsistencies suggest that the structural information near the boundaries of the EAW tomograms is not reliable. However, the location of f1 and f7 in the migrated section and in the traveltime tomogram, expand the fault geometry found in the trench from 5 to 7 faults.

Both types of tomograms indicate LVZs 3*, 4*, 5*, 6, 7* and 8, where the asterisks again denote LVZs that coincide approximately with the location of colluvial wedges known from the trench log extract (a). Smaller offsets between the wedges and the LVZs are mostly due to inaccurate coordinates of the colluvial wedges and smearing effects of the inversion process. LVZ 6 possibly reveals a colluvial wedge associated with the main fault f4 at a depth of 26–39 m, that is 18–21 m below the surface. In order to estimate the timing of the deposition of this LVZ, whether this is a colluvial wedge or a geologic body of other origin, a sedimentation rate profile for the last 25 000 yr is required but had not been established yet to our knowledge. However, it is estimated that the sedimentation rate has not fallen below 1 mm yr^{-1} in the past 25 000 yr (Susan Olig, personal communication), so that 18–21 m of sediment can be deposited in a time frame of 18 000–21 000 yr. Hence, if this LVZ does represent a colluvial wedge, then the earthquake or sequence of earthquakes that created this wedge occurred at most 21 000 yr B.P. However, a confirmation of this hypothetical colluvial wedge and more accurate dating can possibly be obtained by taking and carbon-dating drill samples or by using optical stimulated luminescence methods (Mattson *et al.* 2003).

In (j), two colluvial wedges, associated with two different faults, lie within LVZ 7, where the velocity contrasts are so low that the different events cannot be distinguished. LVZ 8 is located within the bigger low-velocity region, in which we also find LVZ 7 (coll. wedges) and the bioturbated area. Interestingly, with a length of 8 m and a thickness of 4 m the biggest colluvial wedge (the uppermost wedge associated with fault f4) found in the trench, has not been resolved by either tomography method, although it is definitely large enough to be within the resolution capabilities at this shallow depth. However, since the velocities at shallow depth are even slower than the air velocity, as seen in Fig. 7, the velocity contrast between the near surface sediments and the colluvial wedge might be too small (less than 15 per cent), to be detected by the inversion.

LVZs 1 and 9 were detected by EAW inversion (Figs 12i–j) and also lie within the trench log. The trench log describes the location of LVZ 1 as loose sediments that accumulated on top of fault f2, that are not associated with a colluvial wedge. LVZ 9 lies in an area of bioturbation. LVZ 2 was detected only by traveltime tomography. LVZ 2 is located outside the trench log downhill of f1 and could possibly represent a colluvial wedge. However, its rupture time cannot be calculated without taking drill samples, because the surface on a hanging wall is subject to erosion.

Supported by the migrated section, the Pre-Trench tomograms show that waveform tomography and traveltime inversion are capable of locating faults. More difficult is the resolution of the near-surface colluvial wedges at the Mapleton site due to the very low velocity of the surface sediments. However, both synthetic and field data results suggest that waveform inversion provides about twice the resolution of the traveltime tomogram, indicating a better resolution of faults and LVZs. Fig. 13 contains four resolution diamond samples at LVZ 3, 6 (deep wedge) and 9 (bioturbation), and at the location of the biggest colluvial wedge. Except for the bioturbated area, the resolution at those locations is sufficient to resolve the low-velocity structures. At LVZ 9, smearing effects result in a poor resolution in the horizontal (23°).

4.2 Post-trench tomographic results

Fig. 14 shows the results from traveltime inversion of the Post-Trench data and, for comparison, the respective area from the Pre-Trench traveltime inversion (a). Again, the asterisks (*) denote close proximity of the interpreted and actual locations of faults and colluvial wedges known from the trench log extract (Fig. 12).

4.3 Top-bench tomographic result

To determine how the trench excavation affected the velocity distribution in the subsurface, a seismic survey, referred to as the Post-Trench Top-Bench survey, was carried out in September 2003 and coincided with the Pre-Trench line. 48 geophones were centred over the base of the fault scarp (red line) in Fig. 14(c) and 120 shots were evenly distributed along the section. The corresponding area of the Pre-Trench tomogram is shown in (a). As expected, the stress release due to the excavation has decreased the overall seismic wave velocity by about 15 per cent compared to the Pre-Trench tomogram. In order to estimate the effect of the different source/receiver geometries, the

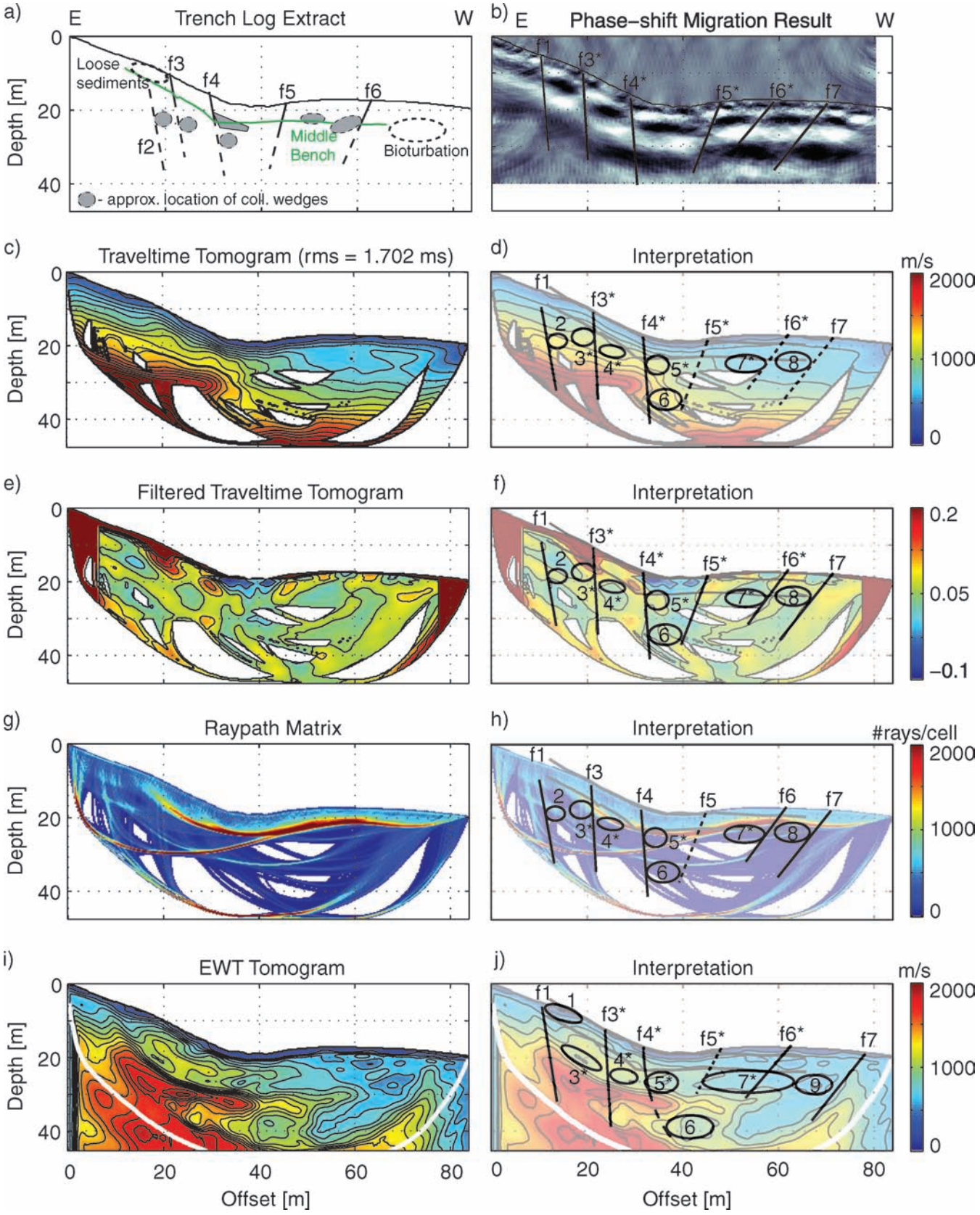

Figure 12. (a) Trench log extract, (b–j) results of the pre-trench data applying (b) phase-shift migration, (c–d) traveltime inversion, (e–f) filtered tomogram of the traveltime inversion, (g–h) raypath matrix, (i–j) early-arrival-waveform inversion, with their respective interpretations on the right panels. The asterisks (*) on the faults and LVZs denote where they coincide with faults and colluvial wedges or bioturbation, respectively, known from the trench log extract. The white line in (i–j) delineates the depth limit of the traveltime tomogram. LVZ 5 represents a possible colluvial wedge. Although both tomograms were able to resolve the main faults and LVZs, EAW tomography resolves the features more clearly.

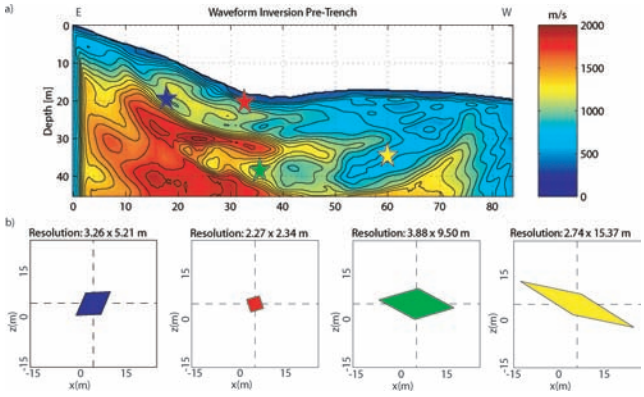

Figure 13. (a) Tomogram of the Pre-Trench line using waveform inversion and (b) resolution diamonds showing the horizontal and vertical resolution at the location of the accordingly color coded stars in (a). The green diamond shows that the vertical extension of the closure of contours is within the resolution limits. The LVZ can be interpreted as a possible colluvial wedge.

Pre-Trench data have been decimated (b) to a source/receiver geometry equivalent to the one of the Top-Bench data set. At both ends of the geophone line, the velocities are higher than in the Pre-Trench tomogram, similar to the higher velocities in the Top-Bench tomogram at the ends of the geophone line. The rays along the edges of the survey are not numerous and thus tend to blur the velocities. Hence, the clear recovery of faults f3* and f5* is partly an artefact due to the edge effect. Fault f4* is not recovered in this tomogram. The excavation of the trench has lowered the seismic velocities and the velocity contrast so that seismic tomography apparently cannot resolve any structures near the free surface.

4.4 Middle-bench tomographic result

Since the Middle-Bench line was not located on the free vertical surface, the effect of the excavation is expected to be smaller, so that the subsurface structure beneath the middle bench should be resolvable. However, the tomogram shown in Fig. 14(d) contains surprisingly little detail. Except for fault f4* and a corresponding colluvial wedge (LVZ 5*), the tomogram does not reveal new information, nor does it support the fault interpretation for the faults f3 and f5 based on the migrated section and on the trench log. Fault f4, however, is clearly resolved, so that the dip angle can be estimated to be as steep as 71° to 80°. Moreover, the location of LVZ 1 coincides with the location of a colluvial wedge, which is associated with fault f4.

4.5 Post-trench Crossbench tomographic results

The Crossbench tomogram theoretically should have the best horizontal resolution of the area between the two benches because many rays have nearly vertical incidence angles. On the other hand, the stress release due to the excavation should have decreased the velocity contrast near the free surface of the trench. As seen in Fig. 14(e), the velocities in the Crossbench tomogram are slower than in the Pre-Trench tomogram, but the inversion was still able to resolve most of the faults. For the first time, two colluvial wedges are resolved as two distinct LVZs 3 and 4. As in the Top-Bench experiment, this tomogram does not reveal fault f4 or its colluvial wedges, which supports the conjecture that the velocity contrast of the fault is too low due to the excavation. This suggests that geophones located

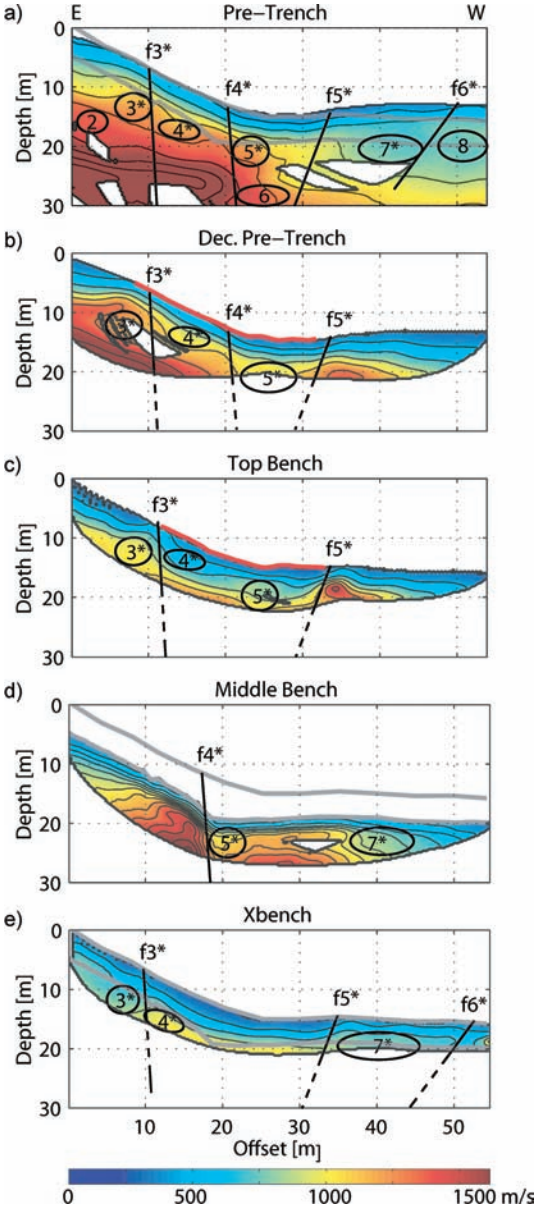

Figure 14. Tomograms of the Post-Trench data and the respective area of the Pre-Trench Tomogram of Fig. 12(c). (a) extract from Pre-Trench tomogram; (b) the resulting tomogram of the Pre-Trench data, after they were decimated to a data set that resembles the source/receiver geometry of the Post-Trench Top Bench survey; (c) Top-Bench tomogram; the good mapping of faults f3 and f5 is party due to the edge effect, which raises the velocities near the ends of the geophone line. The velocities decreased by 15 per cent after the trench excavation. (d) Middle-Bench tomogram; Fault f4 is mapped clearly enough to estimate the fault angle to 71–80°. (e) Cross-Bench tomogram.

in a horizontal well drilled beneath the colluvial wedge could be used for a horizontal seismic profile experiment. The resulting seismic data could possibly be inverted to reliably estimate faults and LVZs.

5 CONCLUSIONS

An overview over the faults and LVZs recovered by each method and data set is given in Table 4. These survey results demonstrate the

Table 4. List of all features resolved in each tomogram (checked with and x). A star denotes where the interpretation of the tomograms agrees with the ground truth. Pre-T, Post-T = Pre-, and Post-Trench, resp., WV, TT = waveform and traveltime inversion, resp., TB, MB, CB = top-, middle-, and cross-bench, resp.

	Pre-T WF	Pre-T TT	Post-T TB	Post-T MB	Post-T CB	Pre-T Migration	Comments
f1	x	x				x	
f2*							
f3*	x	x	x		x	x	
f4*	x	x		x		x	71–80° dip angle
f5*	x	x	x		x	x	
f6*	x	x			x	x	
f7	x	x				x	
LVZ 1	x						Loose sediments
LVZ 2		x					Possible coll. wedge
LVZ 3*	x	x	x		x		
LVZ 4*	x	x	x		x		
LVZ 5*	x	x	x	x			
LVZ 6	x	x					Possible coll. wedge (at most 21.000 years B.P)
LVZ 7*	x	x		x	x		
LVZ 8	x	x					
LVZ 9	x						Bioturbation

capabilities of seismic tomograms and reflection images for identifying nearly all near-surface faults along the megatrench. Both waveform and traveltime tomography resolved four out of five of the known faults based on the migrated section and the trench log and extended their known locations to a depth of 30 m below the surface. Outside the trench log area, the conjectured fault f1 is delineated by all three methods, and fault f7 by migration and traveltime tomography. Both tomography methods resolved four out of five known colluvial wedges. However, both methods did not recover the biggest colluvial wedge that was found in the trench, possibly because the velocity contrast between the wedge and the surrounding material was too small. Other geologic bodies like loose sediments (LVZ1) and an area of bioturbation (LVZ9) mapped in the trench log were resolved as LVZs in the EAW tomogram. Both methods imaged a deep LVZ associated with the main fault at a depth of 18–21 m below the surface, which possibly represents a colluvial wedge. Assuming a constant minimum sedimentation rate of 1 mm yr^{-1} (Susan Olig, personal communication), the colluvial wedge originated at most 21 000 yr ago. Also, the good resolution of the Middle-Bench tomogram allowed an estimate of 71–80° dip angle of fault f4. Waveform tomography prevails over traveltime tomography by showing more details and distinct structures in the subsurface.

The Top-Bench tomogram showed a 15 per cent reduction in the average velocity at the trench face after excavation. This velocity reduction prohibited the recovery of subtle features seen in the Pre-Trench tomogram (Fig. 12c). Synthetic tests demonstrated that the sensitivity of the tomogram to steep topography is reasonably small for the Mapleton site. Results showed that LVZs in the near surface and one at 18 m depth with a 15 per cent velocity contrast were resolved for a simple one-fault model and a more complex model containing six faults. However, areas with sparse ray coverage increase with the number of faults.

These results suggest that velocity tomograms and reflection images can be used to identify some, but not all colluvial wedges, so that a conjectured extension of the earthquake history based on seismic tomography alone is not certain. Also, in this case we cannot distinguish between one colluvial wedge or a package of colluvial wedges containing more than one earthquake event. Additionally, other LVZs due to bioturbation or any other reason obscure the interpretation of colluvial wedges. A major part of the ambiguity in the tomograms is due to the many major faults, which result in an uneven raypath coverage as our synthetic studies show. Hence, seismic trenching will be more successful for simple fault geometries with one synthetic and antithetic fault. However, even under optimal conditions there will be ambiguities in interpretation, so that detected LVZs should be drilled, cored and dated to determine the history of the ancient earthquakes. Nevertheless, we have demonstrated that seismic tomography is able to recover faults. If the quality of the data allows, reflections should be used in order to locate faults more precisely. Because of the improved resolution with waveform tomography, future data should be inverted for waveforms rather than traveltimes. Ambiguity in the tomograms can be reduced if 3-D data are used.

ACKNOWLEDGMENTS

We thank Susan Olig and URS Corporation for their trench results, and Min Zhou for his assistance in the data processing. The research was supported partly by funds from the National Science Foundation Grant 0207372 awarded to R.L. Bruhn and G. T. Schuster. Also, we want to thank our reviewers for their suggestions, which helped to greatly improve this publication.

REFERENCES

Bilham, R., 1985. Subsurface radar imagery of near-surface fractures associated with the Borah Peak earthquake, *USGS Open File Report,* **85-290-A,** 182–194.

Bilham, R. & Seeber, L., 1985. Paleoseismic studies using subsurface radar profiling: Summaries of Technical Reports, vol. XIX, *USGS Open File Report,* **85-22,** 47.

Chow, J., Angelier, J., Hua, J.J., Lee, J.C. & Sun, R., 2001. Paleoseismic event and active faulting; from ground penetrating radar and high-resolution seismic reflection profiles across the Chihshang Fault, eastern Taiwan, *Active subduction and collision in Southeast Asia (SEASIA),* **333**(1–2), 241–259.

Christenson, G.E., 2004. Improving Our Understanding of Earthquake Hazards in Utah, *UGS Survey Notes,* **36**(2), 1–3.

Hill, N.R. & Wuenschel, P.C., 1985. Numerical modeling of refraction arrivals in complex areas, *Geophysics,* **50,** 90–98.

Kanamori, H. & Brodsky, E.E., 2001. The Physics of Earthquakes, *Physics Today,* **54**(6), 34–40.

Lund, W.R., Schwartz, D.P., Mulvey, W.E., Budding, K.E. & Black, B.D., 1991. Fault behavior and earthquake recurrence on the Provo segment of the Wasatch fault zone at Mapleton, Utah County, Utah, *UGMS Special studies* **75**.

Machette, M.N., Personius, S.F., Nelson, A.R., Schwartz, D.P. & Lund, W.R., 1991. The Wasatch fault zone, Utah - segmentation and history of Holocene earthquakes, *J. Struct. Geol.,* **13**(2), 137–149.

Mattson, A., 2004. Tomographic imaging of late Quaternary faulting, Oquirrh Mountains, Utah, *J. geophys. Res.,* **109**(11), 1–19.

Mattson, A., Bruhn, R.L. & Schuster, G.T., 2003. Beneath the trench: High-resolution seismic tomograms and sediment cores applied to paleoseismology, Mercur, Utah, *Abstracts,* GSA Annual Meeting. **35**(6), 581.

McCalpin, J.P., 1996. *Paleoseismology,* Academic Press.

McCalpin, J.P. & Nishenko, S.P., 1996. Holocene Paleoseismicity, Temporal Clustering and Probabilities of Future Large ($M > 7$) Earthquakes on the Wasatch Fault Zone, Utah, *J. geophys. Res.,* **101**(3), 6233–6253.

Meghraoui, M., Camelbeeck, T., Vanneste, K., Brondeel, M. & Jongmans, D. 2000. Active faulting and paleoseismology along the Bree Fault, Lower Rhine Graben, Belgium *J. geophys. Res.,* **105**(6), 12809–13841.

Morey, D. & Schuster, G.T., 1999. Paleoseismicity of the Oquirrh fault, Utah from shallow seismic tomography, *Geophys. J. Int.,* **138,** 25–35.

Nemeth, T., Normark, E. & Qin, F., 1997. Dynamic smoothing in cross-well traveltime tomography: *Geophysics,* **62**, 168–176.

Olig, S., McDonald, G., Black, B., DuRoss, C. & Lund, B., 2004. The Mapleton 'Megatrench', *UGS Survey Notes,* **36**(2), 4–6.

Olig, S., McDonald, G., Black, B., DuRoss, C. & Lund, W.R., 2005. Evidence from the Mapleton Megatrench for more frequent Holocene earthquakes on the Provo segment of the Wasatch fault zone, Utah, *GSA Annual Meeting*, **37**(7), 476.

Qin, F., Luo, Y., Olsen, K.B., Cai, W. & Schuster, G.T., 1992. Finite-difference solution of the eikonal equation along expanding wavefronts, *Geophysics,* **57**, 478–487.

Schwartz, D.P. & Coppersmith, K.J., 1984. Fault Behavior and Characteristic Earthquakes: Examples From the Wasatch and San Andreas Fault Zones, *J. geophys. Res.,* **89**(B7), 5681–5698.

Sheley, D., Crosby, T., Zhou, M., Giacoma, J., Yu, J., He, R. & Schuster, G.T., 2003. 2-D Seismic Trenching of Colluvial Wedges and Faults, *Tectonophysics*, **368,** 51–69.

Sheng, J., 2004. High Resolution Seismic Tomography With the Generalized Radon Transform and Early Arrival Waveform Inversion, *PhD. Thesis*, University of Utah.

Sheng, J. & Schuster, G.T., 2003. Finite-frequency resolution limits of wave path traveltime tomography for smoothly varying velocity models, *Geophys. J. Int.,* **152**(3), 669–676.

Sheng, J., Leeds, A., Buddensiek, M. & Schuster, G.T., 2006. Early arrival waveform tomography on near-surface refraction data, *Geophysics,* **71,** U47–U57.

Smith, D.G. & Jol, H.M., 1995. Wasatch fault (Utah), detected and displacement characterized by ground penetrating radar, *Environ. Eng. Geosci.,* **V1**, 489–496.

Stoffa, P.L., Fokkema, J.T., de Luna Freire, R.M. & Kessinger, W.P., 1990. Split-step Fourier migration *Geophysics,* **55**(4), 410–421.